HHS Public Access

Author manuscript

Neuroimage. Author manuscript; available in PMC 2017 January 01.

Published in final edited form as:

Neuroimage. 2016 January 1; 124(0 0): 612–626. doi:10.1016/j.neuroimage.2015.09.028.

Evaluation of Diffusion Kurtosis Imaging in Ex Vivo Hypomyelinated Mouse Brains

Nathaniel D. Kelm[a,b], **Kathryn L. West**[a,b], **Robert P. Carson**[c,d], **Daniel F. Gochberg**[b,e], **Kevin C. Ess**[c,d], and **Mark D. Does**[a,b,e,f]

[a]Department of Biomedical Engineering, Vanderbilt University

[b]Vanderbilt University Institute of Imaging Science, Vanderbilt University

[c]Department of Pediatrics, Vanderbilt University School of Medicine

[d]Department of Neurology, Vanderbilt University School of Medicine

[e]Department of Radiology and Radiological Sciences, Vanderbilt University School of Medicine

[f]Department of Electrical Engineering, Vanderbilt University

Abstract

Diffusion tensor imaging (DTI), diffusion kurtosis imaging (DKI), and DKI-derived white matter tract integrity metrics (WMTI) were experimentally evaluated ex vivo through comparisons to histological measurements and established magnetic resonance imaging (MRI) measures of myelin in two knockout mouse models with varying degrees of hypomyelination. DKI metrics of mean and radial kurtosis were found to be better indicators of myelin content than conventional DTI metrics. The biophysical WMTI model based on the DKI framework reported on axon water fraction with good accuracy in cases with near normal axon density, but did not provide additional specificity to myelination. Overall, DKI provided additional information regarding white matter microstructure compared with DTI, making it an attractive method for future assessments of white matter development and pathology.

Graphical Abstract

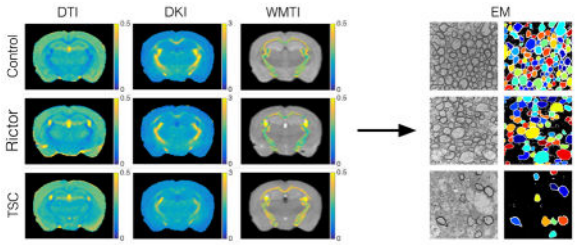

Correspondence should be addressed to: Mark D. Does, Ph.D., 1161 21st Ave South, AA-1105, Nashville, TN 37232-2310, Ph: 615-322-8352, mark.does@vanderbilt.edu.

Keywords

MRI; diffusion; kurtosis; white matter; myelin; quantitative histology

1. Introduction

Abnormal brain myelination is present in many neurological diseases and disorders, such as multiple sclerosis (Allen and McKeown, 1979) and schizophrenia (Davis et al., 2003); therefore, non-invasive assessment of myelin may improve clinical diagnosis and/or insight into treatment of these conditions. At least two magnetic resonance imaging (MRI) methods are established as specific to myelin content—multi-exponential T_2 (MET_2) (MacKay et al., 1994; Menon et al., 1992) and quantitative magnetization transfer (qMT) (Gochberg and Gore, 2007; Koenig et al., 1990; Kucharcyzk et al., 1994; Sled and Pike, 2000)—but clinical application of these methods remains challenging, due to scan time requirements and precision limitations. In contrast, diffusion-weighted MRI (DWI) is widely available and known to be sensitive to tissue microstructure, yet its ability to report on myelination remains an open question.

DWI is based on the sensitization of the acquired MR signal to the random displacement of water molecules, which is greatly influenced by tissue microstructure (e.g., cell membranes, myelin). In three dimensions, DWI can estimate a diffusion tensor (i.e., diffusion tensor imaging – DTI), from which rotationally invariant parameters (e.g., fractional anisotropy and mean, axial, and radial diffusivity – FA, MD, AD, and RD, respectively) can be computed, making it especially applicable in the imaging of tissue with anisotropic microstructure such as white matter (Basser and Jones, 2002; Basser et al., 1994a; 1994b; Beaulieu, 2002; Le Bihan et al., 2001). Although DTI is sensitive to microstructural changes present in many neurological diseases and disorders, it utilizes a mathematical model of diffusion that lacks inherent specificity to any particular component of neuronal microstructure. Additionally, DTI is based upon a Gaussian approximation of the water diffusion displacement probability distribution that assumes free, unrestricted diffusion. This limits the ability of the DTI model to characterize the heterogeneous microstructural environment that comprises brain white matter.

Diffusion kurtosis imaging (DKI) (Hui et al., 2008; Jensen and Helpern, 2010; Jensen et al., 2005; Lu et al., 2006; Wu and Cheung, 2010) is a clinically-applicable extension of DTI with the potential of providing additional information regarding white matter microstructure, including its state of myelination (Cheung et al., 2009). Since its development, DKI has shown promising results in characterizing white matter changes in multiple diseases and disorders, including schizophrenia (Ramani et al., 2007), attention-deficit hyperactivity disorder (Helpern et al., 2011), and medial temporal lobe epilepsy (Lee et al., 2013). DKI is based upon the measurement of the kurtosis (i.e., a deviation from Gaussian) of the water diffusion displacement probability density function. Restrictions to water diffusion present in biological tissue cause the diffusion to become non-Gaussian, making DKI sensitive to heterogeneity in tissue microstructure. Rotationally invariant metrics such as mean, axial, and radial kurtosis (MK, AK, and RK, respectively) can be derived from the kurtosis tensor. Similar to DTI, DKI is based upon a mathematical signal model of diffusion that does not

explicitly model tissue microstructure and lacks inherent microstructural specificity. Additionally, both DTI and DKI utilize generic signal models that do not uniquely characterize multiple tissue compartments, such as intra- and extracellular spaces or crossing fibers. As an alternative to tensor models, biophysical models based on anatomy could provide improved characterization of white matter microstructure.

Fieremans and coworkers recently proposed a biophysical model of white matter based on the DKI framework with the goal of extracting metrics with a direct relationship to specific components of white matter microstructure (Fieremans et al., 2011). This white matter tract integrity (WMTI) model utilizes measurements of apparent diffusion and kurtosis to separate white matter into two compartments: the intra-axonal space and extra-axonal space. In order to accomplish this, the model assumes that a given voxel of white matter consists of parallel fiber bundles, limiting its application to large white matter tracts with minimal crossing fibers. From this model, potentially useful measures such as the axonal water fraction (F_a), intra-axonal diffusivity (D_a, assumed to be entirely parallel to the axon), and axial and radial extra-axonal diffusivities ($D_{e,\parallel}$ and $D_{e,\perp}$) can be computed. It has been hypothesized that D_a and $D_{e,\parallel}$ are associated with axonal integrity and F_a is a potential biomarker of axonal loss (Benitez et al., 2014; Falangola et al., 2014; Fieremans et al., 2013; Fieremans et al., 2012a; 2012b; Hui et al., 2012). Although myelin is not explicitly incorporated into the WMTI model, Fieremans et al. have postulated that $D_{e,\perp}$ (and the related extra-axonal tortuosity) is an indirect measure of myelination (Fieremans et al., 2012a).

The objective of this study was to evaluate the relationship of both DKI and the associated WMTI model with histological measure of white matter microstructure in two hypomyelinated mouse models related to the human genetic disease tuberous sclerosis complex (TSC). These conditional knockout models, *Tsc2* Olig2-Cre CKO (TSC) and *Rictor* Olig2-Cre CKO (Rictor), were chosen because they exhibit varied degrees of hypomyelination. Previously reported TSC models (*Tsc1* Emx1-Cre and *Rictor* Emx1-Cre) showed similar hypomyelination (Carson et al., 2013; Carson et al., 2012). The CKO mice in this study are viable into adulthood and capable of reproduction. High magnification transmission electron microscopy (EM) images of white matter tracts have shown that axon and myelin microstructure appear normal. Additionally, in contrast to the cuprizone mouse model of demyelination utilized in previous diffusion-weighted MRI studies (Song et al., 2005; Sun et al., 2006; Thiessen et al., 2013; J. Zhang et al., 2012), these genetic models are expected to exhibit less or no inflammation or cellular damage and the hypomyelination is mostly uniform in white matter, making them better suited for a study focused on assessing the effects of hypomyelination on MRI contrast. In order to evaluate their relationship with myelin content, we compared DTI, DKI, and WMTI metrics with two established MR measures of myelin, myelin water fraction (MWF) from MET_2 and macromolecular pool-size ratio (PSR) from qMT, as well as quantitative measures of histology.

2. Materials and Methods

2.1 Animal Preparation

All animal studies were completed with the approval of the Vanderbilt University Institutional Animal Care and Use Committee. TSC and Rictor mice were the product of crosses between *Tsc2* or *Rictor* homozygous floxed animals with *Tsc2* or *Rictor* floxed heterozygous; Olig2-Cre hemizygous mice. The resultant CKO genotypes were then: $Tsc2^{F/F}$;Olig2-Cre or $Rictor^{F/F}$;Olig2-Cre. Normal (N = 8), TSC (N = 5), and Rictor (N = 5) P60 mice were euthanized and transcardially perfusion-fixed with 2.5% glutaraldehyde and 2% paraformaldehyde + 1mM Gd-DTPA (Magnevist, Bayer HealthCare, Wayne, NJ, USA) in phosphate-buffered saline (PBS) (Johnson et al., 2002; Karnovsky, 1965). Mouse brains were excised and post-fixed in the same fixative solution at 4°C for a period of 1 week to allow for complete penetration of the fixative. The mouse brains were then placed in PBS + 1mM Gd-DTPA at 4°C for at least 1 week before imaging, with the solution changed out 3 times, in order to wash out residual fixative that reduces the tissue T_2 and image signal-to-noise ratio (SNR) (Shepherd et al., 2009). The addition of 1 mM Gd-DTPA lowered the T_1 of mouse brain to ≈ 400 ms at 15.2T, effectively increasing the SNR efficiency of the MRI acquisition. Although Gd-DTPA remains extracellular for in vivo experiments, previous studies have indicated that Gd-DTPA affects both the intra- and extracellular compartments in fixed ex vivo tissue, and that it has a similar effect on the T_2 of both the myelin water and intra/extra-axonal water pools (Dortch et al., 2010; Purea and Webb, 2006). For imaging, mouse brains were placed in MR-compatible tubes filled with a perfluropolyether liquid (Fomblin, Solvay Solexis, Thorofare, NJ, USA) for susceptibility matching, preventing tissue dehydration, and a signal-free background.

2.2 MRI

Ex vivo mouse brain imaging was performed at bore temperature (17±0.5 °C) on a 15.2T 11-cm horizontal bore Bruker Biospec scanner (Bruker BioSpin, Billerica, MA, USA) using a Bruker 35-mm quadrature volume coil for RF transmission and reception. All three MRI protocols, DKI, MET_2, and qMT, were acquired in a single session with field of view (FOV) = 19.2 × 14.4 × 10.8 mm^3 and matrix size = 128 × 96 × 72 for a nominal isotropic resolution of 150 × 150 × 150 μm^3 in a total overall scan time of ≈ 22 hr.

2.2.1 Diffusion Kurtosis Imaging—Diffusion kurtosis imaging data were acquired using a 3D diffusion-weighted fast spin-echo sequence with repetition time (TR) = 200 ms, echo time (TE) = 19.0 ms, echo spacing (ESP) = 7.1 ms and echo train length (ETL) = 4 (Beaulieu et al., 1993). For excitation and refocusing, non-selective hard pulses were implemented with durations of 125 and 250 μs, respectively. Receiver bandwidth (BW) for signal acquisition = 75 kHz. Diffusion weighting was achieved with gradient pulse duration (δ) = 5 ms, diffusion time (Δ) = 12 ms, prescribed b-values = 3000 and 6000 s/mm^2, 30 directions (Jones et al., 1999), and 2 signal averages with gradient polarity reversal to mitigate background gradient cross-terms (Neeman et al., 1991). The b-values selected were empirically optimized for ex vivo brain imaging and are larger than those used for in vivo brain imaging due to the decreased diffusivity of brain tissue caused by fixation (Sun et al.,

2003). Five b=0 images were collected and averaged. In all, for each brain, 125 3D volumes were collected in a total scan time of ≈ 12 hr.

2.2.2 Multi-exponential T_2—MET_2 data were acquired using a 3D multiple spin-echo sequence with TR = 520 ms, TE = 5.8 ms, 18 evenly spaced echoes with ESP = 5.8 ms, BW = 38.5 kHz, and 6 signal averages in a total scan time of ≈ 6 hr. For excitation and refocusing, non-selective hard pulses were utilized with durations of 160 and 100 μs, respectively. Crusher gradient pairs with amplitudes = 6 G/cm and durations = 428 μs surrounded each refocusing pulse. With the assumption that secondary echoes not excited by the excitation pulse were removed, the observed echo magnitudes could be related to proton density and T_2 using the extended phase graph (EPG) algorithm (Hennig, 1988).

2.2.3 Quantitative Magnetization Transfer—qMT data were acquired using a 3D selective inversion-recovery prepared fast spin-echo sequence (Gochberg and Gore, 2007) with ETL = 8 and ESP = 5 ms. A 1-ms hard inversion preparation pulse was used to selectively invert the free water pool, while macromolecular spins were mostly unaffected. The acquisition was repeated for 15 inversion times (TI) log-spaced from 3.5 to 2000 ms. A constant pre-delay (T_d) of 590 ms was used, resulting in a total scan time of ≈ 3.5 hr.

2.3 Histology

2.3.1 Tissue Preparation—After MRI was completed, normal (N = 6), TSC (N = 4), and Rictor (N = 3) mouse brains were sectioned for histology. A larger sample size was used for the control group due to greater intragroup variation in myelin content compared with the CKO groups. Following a mid-sagittal cut, four sections of tissue each containing a desired white matter region of interest (ROI), the midbody of the corpus callosum (MidCC), genu (GCC), splenium (SCC), and anterior commissure (AC), were sectioned in the sagittal plane, as shown in Fig. 1a. Tissue sections were placed in 1% osmium tetroxide in cacodylate buffer for 1 hr and dehydrated in graded ethanol. Then, tissue sections were embedded in epoxy resin and 1 μm thick sections were cut and stained with 1% toluidine blue. Using images of these thick sections, a 500 × 500 μm^2 ROI was manually selected from each tissue block with the aid of a standard mouse brain atlas (Paxinos and Franklin, 2001) and 70 nm ultra-thin sections were cut from the ROI for EM. The MidCC ROI was chosen as the portion of the corpus callosum just superior to the anterior part of fornix where its fibers bend to travel inferiorly from the corpus callosum (Bregma −0.7 mm). The GCC and SCC ROIs were selected as the most anterior (Bregma 1 mm) and posterior (Bregma −2.5 mm) sections of the corpus callosum, respectively. The AC ROI encompassed the entirety of the anterior commissural tract crossing through the mid-sagittal plane and was located just anterior to the fornix at Bregma 0.2 mm. Data from 1 TSC MidCC section and 1 TSC GCC section were removed from analysis due to corruption of these sections during histology processing, so a fourth TSC brain was added to ensure that there were at minimum 3 samples of each ROI.

2.3.2 Transmission Electron Microscopy—EM images of ultra-thin sections were collected with an FEI Tecnai T12 electron microscope (FEI, Hillsboro, OR, USA) at various magnifications. From these images, measurements of axon diameter (inside the myelin) (d_a),

myelin thickness (z_m), g-ratio (g), axon density (ρ_a), histologic myelin fraction (f_m), and histologic axon fraction (f_a) were performed in MATLAB (Mathworks, Natick, MA, USA). In order to avoid confusion, all histology measures are identified with lowercase variables and all MR-derived metrics are reported as upper-case variables or acronyms.

Using images collected at 6500x (≈ 3 per white matter tract, Suppl. Fig. 1), axon density was measured by manual counting the number of myelinated axons within the given area. Four 15000x images were acquired from the same area as each 6500x image (≈ 12 total per tract, Fig. 1b and Suppl. Fig. 1). Since these images could generally be described by a bimodal histogram, segmentation was performed by applying a threshold located at the local minimum between the two peaks of the histogram in order to distinguish between myelin (white) and non-myelin (black) pixels (Fig. 1c), which provided a measure of myelin fraction for each image. In the segmented images, N individual axons were manually identified (Fig. 1d, $N \approx 300$ for control and Rictor mice, and $N \approx 75$ for TSC mice, which had a much lower axon density) and from each: i) a region-growing algorithm computed the cross-sectional area (Fig. 1e) which was then converted to a diameter assuming circular geometry, and ii) myelin thickness was determined by taking the average of measurements along 2 different axes (Fig. 1e). The g-ratio, the ratio between the inner and outer diameters of a myelinated axon, was calculated for the i^{th} axon as:

$$g_i = \frac{d_{a,i}}{d_{a,i} + 2z_{m,i}}. \quad (1)$$

For accurate axon diameter measurements, only axons that were entirely visible within the image were selected for measures of d_a, z_m, and g. A measure of histologic axon fraction for each image was then computed by summing the cross-sectional areas for all myelinated axons, including those that were partially visible.

For group analysis of histological measures, the mean and standard error of each measure was taken across all analyzed EM images for each group (15000x for d_a, z_m, g, f_m, and f_a, 6500x for ρ_a). For a conservative estimate of error, the standard error was based on the number of different brains in the group as opposed to the number of images used. Histological measures were then compared between the control and knockout groups using a Wilcoxon rank-sum test.

2.4 Data Analysis

Image data were analyzed using in-house written code in MATLAB (Mathworks, Natick, MA, USA). For DWI analysis, 3D k-space data were zero-padded 2x in each direction before reconstruction, resulting in a working isotropic image resolution of 75 μm. DTI analysis was performed by estimating diffusion tensors voxel-wise using a linear least squares approach and calculating the DTI indices FA, MD, AD, and RD from these tensors. Using data acquired with too high of b-value can cause systematic errors in DTI measures, so the b = 6000 s/mm^2 DWI data were excluded from the DTI analysis alone. For DKI analysis, diffusion and kurtosis tensors were estimated voxel-wise using a constrained linear

least-squares approach (Tabesh et al., 2011) and DKI indices MK, AK, and RK were calculated.

The following WMTI equations (Eqs. 2–4) and their derivations first appeared in Fieremans et al. (Fieremans et al., 2011). First, F_a was estimated voxel-wise as:

$$F_a = \frac{K_{max}}{K_{max}+3}, \quad (2)$$

where K_{max} is the maximum kurtosis over all directions derived from the kurtosis tensor. Then, compartmental diffusion coefficients along the i^{th} diffusion direction for the intra- and extra-axonal spaces, $D_{a,i}$ and $D_{e,i}$ respectively, were calculated using the diffusion coefficient D_i and kurtosis coefficient K_i:

$$D_{a,i} = D_i \left[1 - \sqrt{\frac{K_i(1-F_a)}{3F_a}}\right], \quad (3)$$

$$D_{e,i} = D_i \left[1 + \sqrt{\frac{K_i F_a}{3(1-F_a)}}\right]. \quad (4)$$

From these diffusion coefficients, intra- and extra-axonal diffusion tensors $\mathbf{D_a}$ and $\mathbf{D_e}$, respectively, were computed and rotationally invariant parameters for each compartment were derived similar to conventional DTI analysis. WMTI metric D_a was computed voxel-wise as the trace of $\mathbf{D_a}$. $D_{e,\parallel}$ and $D_{e,\perp}$ were calculated voxel-wise as the primary eigenvalue of $\mathbf{D_e}$ and the average of the secondary and tertiary eigenvalues of $\mathbf{D_e}$, respectively.

The MET_2 analysis was performed using the freely available multi-exponential relaxation analysis tool for MATLAB (vuiis.vanderbilt.edu/~doesmd/MERA/MERA_Toolbox.html). Echo magnitudes from each image voxel were fitted via a conventional linear inverse approach (Whittall and MacKay, 1989) by non-negative least-squares (NNLS) (Lawson and Hanson, 1974) to the sum of signals from 100 logarithmically spaced T_2 components, as defined by the EPG algorithm and spanning TE/2 to 500 ms in the T_2 domain, similar to previous work (Prasloski et al., 2012). The spectra were regularized using a minimum curvature constraint with a constant conservative regularization (μ = 0.002) across all voxels. For each voxel, the sum of signal with T_2 < 17 ms relative to total signal was defined as the MWF. For qMT analysis, the 15 signal magnitudes acquired with varying TI were fitted voxel-wise to a five-parameter biexponential model as described previously (Gochberg and Gore, 2007), from which the ratio of macromolecular to free pool magnetization (or PSR) was calculated.

For group analysis, b=0 images were registered to a representative normal mouse brain using a rigid affine transformation followed by a non-rigid deformable demons registration (Thirion, 1998). DTI, DKI, WMTI, MWF, and PSR parameter maps were then registered using the same transformations derived from the b=0 registration. Referencing a standard mouse brain atlas (Paxinos and Franklin, 2001), ROIs were manually delineated on 2D

cross-sections for 6 white matter regions: MidCC, GCC, SCC, AC, external capsule (EC), and internal capsule (IC). For direct comparison to the histology ROIs, the MidCC, GCC, SCC, and AC ROIs were drawn on a mid-sagittal cross-section at Bregma −0.7 mm, 1 mm, −2.5 mm, and 0.2 mm, respectively. The EC and IC ROIs were drawn on a coronal cross-section at Bregma −1.7 mm and were only included in analyses involving MR metrics alone. For the WMTI analysis, a small number of voxels (< 1% of all WM voxels used in this analysis) exhibited abnormally high $D_{e,\perp}$ (> 1 $\mu m^2/ms$; mean ± SD of remaining WM voxels $D_{e,\perp}$ = 0.27 ± 0.07 $\mu m^2/ms$) and were not included in subsequent analysis. Comparisons of DTI, DKI, and WMTI indices between the control group and knockout groups were then made for each ROI using a Wilcoxon rank-sum test. Using the ROI means for each individual mouse brain, linear correlations were determined between DTI, DKI, and WMTI parameters and both MR measures of myelin and histologic measures with multiple comparisons correction performed using a simple Bonferroni correction.

3. Results

3.1 Histology

Figure 2 displays electron micrographs, along with their corresponding segmentations, of the splenium from normal, Rictor, and TSC brains. In comparison to the normal brain, the Rictor brain visually showed minor decreases in myelin thickness and myelinated axon density, while the TSC brain showed a much greater decrease in myelinated axon density. Table 1 displays group means and standard errors of all histology measures for each ROI. Significant differences compared to the control group are identified by * ($p < 0.05$), ** ($p < 0.01$), and *** ($p < 0.001$). The g-ratios for the control group were similar to those reported in previous studies of normal mouse brain ($g \sim 0.8$) (Mason et al., 2001). Compared to the control group, the TSC group exhibited major decreases in f_m, f_a and ρ_a in all ROIs. There were also significant decreases in z_m in the MidCC and GCC. The TSC group showed significant increases in d_a and g for all ROIs. Compared to the control group, the Rictor group had significant decreases in f_m, z_m, and ρ_a and significant increases in g for all ROIs. Also, the Rictor group showed significant increases in d_a in the GCC, SCC, and AC and a significant decrease in f_a for the GCC. Overall, as anticipated, the microstructural differences between the Rictor and control groups were fewer and less extreme than those observed between the TSC and control groups.

3.2 MRI

Typical white matter SNR of the DWI b=0 images was ≈ 150, calculated as the ratio of the signal amplitude to the standard deviation of the background noise. Approximate mean signal attenuations for the b = 3000 and 6000 s/mm^2 acquisitions were 44% and 57%, respectively (assuming a diffusivity of 0.25 $\mu m^2/ms$ and a kurtosis of 1.75, taken from approximate MD and MK of white matter in this study). The high SNR of the DWI scan resulted in high-precision estimates of DTI parameters in white matter, with estimated standard deviations of < 0.01 and < 0.01 $\mu m^2/ms$ for FA and MD, respectively (Landman et al., 2007). For the MET_2 acquisition, white matter SNR of the first echo image was ≈ 600, and for the qMT acquisition, SNR of the longest inversion time image was ≈ 250. These high SNR acquisitions provided high-precision estimates of both MWF and PSR in white

matter. Representative T_2 spectra from a single MidCC voxel for each group are shown in Suppl. Fig. 2. Intra/extra-axonal water T_2s in the MidCC for the control, Rictor, and TSC groups were 36.2 ± 0.4 ms, 39.4 ± 0.9 ms, and 40.6 ± 1.1 ms (mean ± SEM), respectively. Myelin water T_2s in the same region were 5.4 ± 0.3 ms, 5.0 ± 0.2 ms, and 5.8 ± 0.5 ms for the control, Rictor, and TSC groups, respectively.

3.3 DTI

Representative coronal parameter maps for the DTI indices FA, MD, AD, and RD from each of the three groups are shown in Fig. 3. Compared with the control group, the knockout groups had a decrease in FA and increase in MD and RD of white matter. As anticipated, these differences were more apparent for the TSC group compared with the Rictor group, due to more severe hypomyelination present in the TSC brains. Changes in white matter AD between the three groups were not visually apparent. DTI parameter maps for the sagittal and axial orientations can be seen in Suppl. Figs. 3 and 4, respectively.

Figure 4 shows group comparisons of FA, MD, AD, and RD for 6 white matter ROIs. Compared to the control group, the Rictor group showed no significant differences in FA and AD and significant increases in MD for the anterior commissure and RD for 2 of the 6 ROIs (i.e., the splenium and anterior commissure). The TSC group exhibited significant decreases in FA for 5 of the 6 ROIs, significant increases in AD for 4 of the 6 ROIs, and significant increases in MD and RD for all 6 ROIs examined. There were more WM regions with significant differences in MD and RD than FA and AD, indicating that MD and RD were overall more sensitive than FA and AD to the hypomyelination present within the knockout models. Additionally, DTI parameters were unable to distinguish the Rictor group from the control group (significant differences in MD and RD for only 1 and 2 ROIs, respectively).

3.4 DKI

Representative coronal parameter maps for the DKI indices MK, AK, and RK from each of the three groups are shown in Fig. 5. Compared with the control group, the knockout groups showed a decrease in MK and RK of white matter. Similar to the DTI results, these differences were more apparent for the TSC group compared with the Rictor group. There were minimal changes in white matter AK between the three groups. Sagittal and axial DKI parameter maps are shown in Suppl. Figs. 5 and 6, respectively.

Group comparisons of MK, AK, and RK for 6 white matter ROIs are described in Fig. 6. When compared to the control group, the Rictor group had significant decreases in MK for 4 of 6 ROIs and RK for 4 of 6 ROIs with no significant differences in AK. Significant decreases in MK and RK for all 6 ROIs were seen in the TSC group. For AK of the TSC group, there were significant increases in the GCC and AC and significant decreases in the EC and IC. Since most ROIs showed significant differences in MK and RK, this indicates that MK and RK were highly sensitive to changes in myelination present in the two knockout models. Additionally, significant decreases in MK and RK for the Rictor group present in most white matter ROIs indicate an increased sensitivity of these metrics to myelination compared with DTI metrics.

3.5 WMTI

Figure 7 shows representative parameter maps for the WMTI metrics F_a, D_a, $D_{e,\parallel}$, and $D_{e,\perp}$ from each of the three groups. Since the WMTI model is only valid for white matter, WMTI parameter values for white matter voxels (voxels with FA > 0.35 in a control brain) were overlaid on the b=0 image. Compared with the control group, the knockout groups exhibited a major decrease in F_a and a minor increase in $D_{e,\perp}$ of white matter. As expected, these differences were more apparent for the TSC group compared with the Rictor group. Changes in D_a and $D_{e,\parallel}$ between the control and knockout groups were not visually apparent. Suppl. Figs. 7 and 8 contain WMTI parameter maps in the sagittal and axial planes, respectively.

Group comparisons of F_a, D_a, $D_{e,\parallel}$, and $D_{e,\perp}$ for 6 different white matter ROIs are represented by bar plots in Fig. 8. The Rictor group showed significant decreases in F_a for 5 of 6 ROIs when compared to the control group. No significant differences in D_a, $D_{e,\parallel}$, and $D_{e,\perp}$ existed between the control and Rictor groups. For the TSC group, there were significant decreases in F_a and significant increases in $D_{e,\perp}$ for all 6 ROIs. Also, the TSC group had significant increases in D_a for 1 ROI (i.e., the internal capsule) and in $D_{e,\parallel}$ for 2 ROIs (i.e., the external and internal capsules). With significant differences in F_a present in most ROIs, these results indicate that F_a was highly sensitive to microstructural changes present within the CKO models. In comparison, $D_{e,\perp}$ was less sensitive and unable to distinguish between the control and Rictor groups.

3.6 Linear Correlation Analysis

Linear correlation analysis was performed across all individual animals and all ROIs. Figure 9 contains scatter plots displaying linear correlations between DTI metrics and 3 different measures of myelin, with each point representing an ROI mean from a single animal. None of the DTI parameters correlated with MWF. FA and RD showed significant correlations with PSR, but these were weak with the strongest being between RD and PSR ($r^2 = 0.14$). There were moderate correlations between DTI parameters and histologic myelin fraction, with $r^2 = 0.35$ and 0.37 for correlations MD-f_m and RD-f_m, respectively.

Similar to Fig. 9, Fig. 10 shows linear correlations between DTI metrics and histologic measures of axon diameter, myelinated axon density, histologic axon fraction, and g-ratio. FA did not have any significant correlations, while MD and RD showed moderate to strong correlations with all four histology measures, the strongest being between MD and f_a ($r^2 = 0.44$). For Figs. 9 and 10, AD is not shown due to it not showing any significant correlations.

Linear correlations between DKI metrics and 3 unique measures of myelin are shown in Fig. 11. Both MK and RK correlated significantly with MWF and PSR, with the strongest correlations being MK and RK with PSR ($r^2 = 0.27$ and 0.25, respectively). Also, MK and RK correlated strongly with f_m ($r^2 = 0.48$ and 0.49, respectively). All correlations between DKI metrics MK and RK and the myelin measures were stronger than the corresponding correlations between DTI metrics MD and RD and the same myelin measures.

Scatter plots displaying linear correlations between DKI metrics and the histologic measures of axon diameter, myelinated axon density, axon fraction, and g-ratio are shown in Fig. 12.

MK and RK had strong correlations with all four histologic measures, the strongest being between MK and g-ratio ($r^2 = 0.46$). Correlation strengths between DKI metrics and d_a, ρ_a, and f_a were similar to those observed with DTI metrics. However, correlations with g-ratio for MK and RK were much stronger than those observed for MD and RD. For Figs. 11 and 12, AK is not shown because there were no significant correlations observed with this metric.

Linear correlations between WMTI metrics and 3 different measures of myelin are shown in Fig. 13. F_a correlated significantly with MWF and PSR ($r^2 = 0.14$ and 0.23, respectively). A strong correlation existed between F_a and histologic myelin fraction ($r^2 = 0.58$). $D_{e,\perp}$ did not correlate with any of the 3 myelin measures. Figure 14 shows scatter plots with linear correlations between WMTI indices and histologic measures of axon diameter, myelinated axon density, axon fraction, and g-ratio. F_a exhibited strong correlations with all four histology measures, the strongest being between F_a and ρ_a ($r^2 = 0.55$). $D_{e,\perp}$ did not exhibit any significant correlations with these histology metrics. For Figs. 13 and 14, D_a and $D_{e,\parallel}$ are not shown because there were no significant correlations observed with these metrics.

Table 2 summarizes the results of the correlation analysis, showing the r^2 values for all significant correlations of DTI, DKI, and WMTI metrics with myelin and histology measures. A more detailed analysis of the relationships between histology and both MET_2 and qMT data will be reported independently.

4. Discussion

The quantitative histology data shown in Table 1 indicate that both the Rictor and TSC knockout models show hypomyelination, with the TSC model exhibiting an almost complete lack of myelinated axons. The more subtle change in myelination present in the Rictor model (in contrast to the TSC and cuprizone models) is beneficial in evaluating MRI methods and their ability to report on varied levels of myelination that may occur during development or de/remyelinating pathologies. These results agree with previous studies showing that TSC and Rictor knockouts exhibit abnormal myelination, with the TSC mice portraying a more severe abnormal phenotype (Carson et al., 2013; Carson et al., 2012). However, this study is the first to report quantitative histological measures of axons and myelin content (e.g., axon diameter, myelin thickness, histologic myelin fraction) for these specific mouse models.

The DTI results in Figs. 3 and 4 showed that hypomyelination resulted in decreases in white matter FA and increases in MD and RD, with fewer changes in AD. These results agree with previous studies stating that a decrease in myelination causes an increase in radial diffusivity but minimal changes in axial diffusivity (Song et al., 2005; Song et al., 2002). However, DTI metrics mostly did not detect differences between the control and Rictor groups, indicating an inability of DTI to distinguish subtle changes in myelin thickness and myelinated axon density. The DKI results in Figs. 5 and 6 showed that hypomyelination caused decreases in MK and RK with minimal changes in AK. This is similar to the DTI results in that changes in myelination caused changes in radial kurtosis but not axial kurtosis. In contrast to DTI metrics, significant differences in MK and RK between the

control and Rictor groups were present in most ROIs, indicating higher sensitivity to changes in myelin thickness and myelinated axon density compared with DTI.

Because inter-animal variability within each group was approximately an order of magnitude greater than the variability of the DTI metrics themselves, increasing the image SNR in this case would have little effect on the group-wise comparisons. In other words, in the hypothetical case that twice as many acquisitions of a single b-value shell were utilized instead of two shells, the DTI metrics would still prove to be less sensitive to the changes in tissue microstructure than the DKI metrics. These results agree with a previous study that showed that DKI was more sensitive than DTI to changes present in a rat brain maturation model (Cheung et al., 2009). Also, these results make intuitive sense because the assessment of non-Gaussian diffusion in DKI provides more information about the effects that tissue microstructure have on water diffusion and therefore is more sensitive to microstructural changes. This emphasizes the utility of moving towards a higher order diffusion signal model, such as the DKI model, for microstructural assessment.

The WMTI results in Figs. 7 and 8 showed that hypomyelination caused decreases in F_a, increases in $D_{e,\perp}$, and minimal changes in D_a and $D_{e,\parallel}$. These results agree with previous hypotheses stating that F_a is sensitive to axonal loss, $D_{e,\perp}$ increases with reduced myelination, and D_a and $D_{e,\parallel}$ are mostly unaffected by changes in myelination (Fieremans et al., 2012a). Similar to the DKI results, F_a was significantly different between the control and Rictor groups in most ROIs. This was expected since the estimation of F_a is closely related to radial kurtosis. However, even though significant increases in $D_{e,\perp}$ between the control and TSC groups were found for all ROIs, there were no significant differences in $D_{e,\perp}$ between the control and Rictor groups. This result indicates that $D_{e,\perp}$ was not as sensitive to less extreme changes in myelin thickness and myelinated axon density as conventional DKI metrics.

The linear correlation analysis was performed across all individual mouse brains from the 3 groups and all of the WM ROIs analyzed. The two different hypomyelinated mouse models were utilized to create variation in white matter microstructure for the purpose of evaluating DWI metrics and to allow for meaningful correlations. There was not enough variation within an ROI and within each group to provide any correlation. Figures 9 and 10 showed that DTI metrics MD and RD did have some correlation with myelin content and other histologic parameters, including axon density. Some level of correlation is expected since MD and RD were shown to be sensitive to changes in myelination and other microstructural changes. Figures 11 and 12 showed that DKI parameters MK and RK exhibited strong correlations with myelin content and other histologic measures, such as axon density and g-ratio. Not only were DKI metrics more sensitive to changes in myelination compared with DTI as shown by the ROI analysis, but they also exhibited stronger correlations to myelin content than conventional DTI. MK and RK showed significant correlations with each metric examined except for myelin thickness, indicating the limited specificity of these DKI measures. However, their correlations with myelin-related metrics (e.g., myelin fraction, g-ratio) were stronger than those shown with axon diameter, a measure that is mostly independent of myelin content.

Myelin is not explicitly modeled by the DKI framework, yet our results indicate that a strong relationship exists between DKI metrics and myelin content. This is not to say that DKI metrics are or should be more specific to myelin compared with other MR measures that explicitly model myelin, such as MWF and PSR. However, reporting on myelin content is just one potential use for DKI among others due to its high microstructural sensitivity and relative ease of acquisition.

Figures 13 and 14 showed that WMTI metric F_a correlated strongly with myelin content and other histologic measures, such as axon density, axon fraction, and g-ratio. The correlation with axon density and fraction is in agreement with previous work stating that F_a reports on axonal loss (Fieremans et al., 2012a). Whereas the correlations with axon density and axon fraction are intuitive, the correlation with myelin fraction is not straightforward. In this study, a decrease in myelinated axon density is the main component of both decreased axon fraction and myelin fraction, which explains the close relationship between F_a and f_m. Although Fig. 14 suggests that F_a overestimated the true axon fraction by ~50%, note that F_a in the WMTI model is axon water fraction and the myelin water is presumed silent in DWI due to its short T_2. Comparing F_a to $f_a/(1-f_m)$ (not shown), we see that F_a overestimated axon water fraction by only ~10% in control and Rictor mice, making it a reasonably accurate model parameter for small variations from normal. For TSC mice, which histology showed to have near zero myelinated axons, F_a clearly overestimates the water fraction of myelinated axons; however, if unmyelinated axons were also included in this analysis, the correspondence might be closer.

In contrast, $D_{e,\perp}$ did not correlate with the other myelin measures utilized in this study (Fig. 13). Previous work by Fieremans and coworkers (Fieremans et al., 2012a) suggested that $D_{e,\perp}$ reports on changes in myelin thickness, even in the presence of axonal loss. Even though the main difference between the control and CKO groups was a decrease in myelinated axon density, significant decreases in myelin thickness were also present and should have caused increases in $D_{e,\perp}$ in both the Rictor and TSC groups based on this previous hypothesis. However, $D_{e,\perp}$ did not correlate with myelin thickness and was not especially sensitive to microstructural changes between the control and CKO groups. Also, from the correlation plots in Figs. 9–14, it was shown that there were some deviations in DWI metrics between WM regions (e.g., higher MK and RK in the genu of the control mouse brains, represented by the green dots) that were not explained by any one histological parameter used in this study, suggesting other microstructural contributions to these measures.

Although potentially useful for elucidating the relationship between DKI and tissue microstructure, previous comparisons of DKI and associated metrics with histological measures have been limited. One study compared DKI metrics to myelin basic protein immunohistochemistry in a Huntington's disease rat model at two different developmental ages, observing that increases in myelin basic protein stain intensity corresponded with decreases in MD and RD and increases in MK and RK (Blockx et al., 2012). Another study examined the relationship between both DKI and WMTI with immunohistochemistry metrics in a cuprizone mouse model of demyelination, finding that solochrome staining (a stain for myelin) correlated with MK, AK, RK, F_a, D_a, and $D_{e,\perp}$ in the cuprizone group

(Falangola et al., 2014). However, there have been no previous comparisons of DKI or WMTI to direct quantitative histologic measures of axons and myelin content, such as axon diameter, myelin thickness, and histologic myelin fraction. Similar to this work, previous studies have compared DTI metrics FA and RD with myelin measures derived from MET_2 and qMT and found modest correlations between these measures (Mädler et al., 2008; Stikov et al., 2011; Thiessen et al., 2013). However, there have been no prior studies assessing DKI or WMTI metrics in white matter through comparisons with other MR metrics specific to myelin, such as myelin water fraction and macromolecular pool-size ratio. Although histological analysis is difficult and can be susceptible to a variety of error sources, general agreement between the comparisons of DWI metrics with histology, MWF, and PSR support the histological analysis in this study.

There are certain limitations to using diffusion signal models such as DTI and DKI to describe white matter microstructure. Although DKI is sensitive to tissue heterogeneity within a voxel, particularly the mixture of restricted and unrestricted water compartments; the DKI model does not specifically characterize multiple tissue compartments present within white matter. On the other hand, multi-compartment tissue models of diffusion, such as CHARMED (Assaf et al., 2004), AxCaliber (Assaf et al., 2008), ActiveAx (Alexander et al., 2010), NODDI (H. Zhang et al., 2012), and WMTI, seek to derive specific information about tissue components such as intra- and extracellular spaces, axon diameter, axon alignment, axon density, and myelin content. However, these biophysical tissue models each come with their own limitations and biases because they require assumptions about the underlying tissue composition and generally result in lower precision parameters resulting from fitting data to nonlinear models. It remains an open question as to whether signal-based or tissue-based diffusion models provide better assessment of tissue microstructure from a practical standpoint. For this study, application of the biophysical WMTI model provided good estimates of axonal water fraction for control and Rictor mice, but did not provide additional specificity to myelination.

Although the WMTI model does not explicitly incorporate myelin, previous studies have hypothesized its relationship to myelin content (Benitez et al., 2014; Falangola et al., 2014; Fieremans et al., 2012a). This hypothesis is formed on the idea that the presence of myelin will have an effect on the tortuosity of the extra-axonal space or more specifically, the diffusion of extra-axonal water perpendicular to the axons ($D_{e,\perp}$). Other multi-compartment diffusion models, including CHARMED, AxCaliber, ActiveAx, and NODDI (Alexander et al., 2010; Assaf et al., 2008; Assaf et al., 2004; H. Zhang et al., 2012), do not explicitly model myelin, yet they also measure or incorporate the extracellular tortuosity as a part of the model. However, the WMTI model is the first of these used to make inferences concerning myelin content. Unexpectedly, in this study, $D_{e,\perp}$ did not demonstrate correlations with myelin content, bringing into question its utility as a biomarker of myelination.

For this study, the histology measures collected were primarily focused on changes in myelin due to the expected changes observed in the CKO mice. It was shown that axial DWI metrics remained mostly unchanged in these models, as expected. Therefore, a different animal model demonstrating changes in axon microstructure would be more appropriate for

the assessment of axial DWI measures. One microstructural feature not measured in this study that is potentially important in determining DWI contrast is the extra-axonal space fraction. This metric is difficult to measure from EM because it is small and not easily discriminated from unmyelinated axon space. For this study we postulate that it is not a critical factor in determining differences in the DWI measures because neither the TSC nor Rictor model is expected to involve much inflammation.

It is also important to recognize that this MR study was performed on ex vivo mouse brain. Ex vivo tissue has been shown to exhibit decreased diffusivity and increased kurtosis due to chemical fixation (Hui et al., 2008; Sun et al., 2003). Additionally, the choice of fixative has been shown to have an effect on the relaxation and diffusion properties of tissue (Shepherd et al., 2009), and tissue preparation may result in shrinking or distortion that can influence the derived histological measures (Fox et al., 1985). Thus, one should be cautious about using the findings here to interpret in vivo measures of diffusion and kurtosis in white matter.

Comparison between MR metrics and EM-derived histology metrics also has inherent limitations. Matching up ROIs between the two imaging modalities is a difficult process, so utilizing anatomical landmarks that are clearly visible from both the MR image and the histology thick section is important. Even if the ROI is matched with high accuracy, the thickness of the histology section is still much smaller than the MR imaging resolution, which prevents an exact correspondence of the microstructure morphology present in the EM data with that contained in an MR voxel. Also, it is important to note that, for this study, the total FOV sampled for each EM section is still a small fraction of the size of a single MR voxel, so the intra-tract variability must be considered when choosing the amount of EM data required for comparison to MR data.

Selection of appropriate b-values is especially important for DKI studies. Higher b-values than those used in conventional in vivo DTI are necessary in this study both due to the use of ex vivo tissue and to increase sensitivity of the DWI signal to kurtosis. However, the maximum b-value used must also be carefully determined, as using too high of b-values can cause systematic errors in DKI metrics (Jensen and Helpern, 2010). The wide range of diffusivity and kurtosis values present in ex vivo mouse brain make b-value optimization difficult, and in this study for example, there were still some voxels in the genu that needed even larger b-values for more accurate assessment of DKI and WMTI metrics.

5. Conclusions

DKI was demonstrated to have greater sensitivity to changes in myelination compared with conventional DTI. Additionally, through comparisons with other MR measures of myelin and quantitative histology, DKI metrics MK and RK were shown to have stronger correlations with myelin content compared with DTI metrics. Thus, if sufficient time is available for the acquisition of two shells of DWI data, then DKI is preferred over DTI because it provides greater sensitivity to changes in tissue microstructure. Application of the biophysical WMTI model provided reasonably accurate estimates of axon water fraction for

near normal microstructure, but the associated extra-axonal diffusion characteristics did not report on any measure of myelination.

Supplementary Material

Refer to Web version on PubMed Central for supplementary material.

Acknowledgments

Grant sponsors: NIH R01 EB001744, NIH 5K08 NS050484, NIH T32 EB014841, NIH S10 RR029523

The authors thank Brittany Parker for technical assistance with animal husbandry, Sophia Swago for assistance with EM measurements, and Janice Williams, Ph.D., of the VUMC Cell Imaging Shared Resource for assistance with microscopy.

Abbreviations

AC	anterior commissure
AD	axial diffusivity
AK	axial kurtosis
CKO	conditional knockout
d_a	axon diameter
D_a	intra-axonal diffusivity
$D_{e,\parallel}$	extra-axonal axial diffusivity
$D_{e,\perp}$	extra-axonal radial diffusivity
DKI	diffusion kurtosis imaging
DTI	diffusion tensor imaging
DWI	diffusion-weighted MRI
EC	external capsule
EM	transmission electron microscopy
EPG	extended phase graph
FA	fractional anisotropy
f_a	histologic axon fraction
F_a	axonal water fraction
f_m	histologic myelin fraction
FOV	field of view
g	g-ratio
GCC	genu
IC	internal capsule

MD	mean diffusivity
MET$_2$	multi-exponential T_2
MidCC	midbody of the corpus callosum
MK	mean kurtosis
MR	magnetic resonance
MRI	magnetic resonance imaging
MWF	myelin water fraction
PSR	macromolecular pool-size ratio
qMT	quantitative magnetization transfer
ρ_a	myelinated axon density
RD	radial diffusivity
RK	radial kurtosis
ROI	region of interest
SCC	splenium
SEM	standard error of the mean
SNR	signal-to-noise ratio
TSC	tuberous sclerosis complex
WM	white matter
WMTI	white matter tract integrity
z_m	myelin thickness

References

Alexander DC, Hubbard PL, Hall MG, Moore EA, Ptito M, Parker GJM, Dyrby TB. Orientationally invariant indices of axon diameter and density from diffusion MRI. Neuro Image. 2010; 52:1374–1389.10.1016/j.neuroimage.2010.05.043 [PubMed: 20580932]

Allen IV, McKeown SR. A histological, histochemical and biochemical study of the macroscopically normal white matter in multiple sclerosis. J Neurol Sci. 1979; 41:81–91. [PubMed: 438845]

Assaf Y, Blumenfeld-Katzir T, Yovel Y, Basser PJ. AxCaliber: a method for measuring axon diameter distribution from diffusion MRI. Magn Reson Med. 2008; 59:1347–1354.10.1002/mrm.21577 [PubMed: 18506799]

Assaf Y, Freidlin RZ, Rohde GK, Basser PJ. New modeling and experimental framework to characterize hindered and restricted water diffusion in brain white matter. Magn Reson Med. 2004; 52:965–978. [PubMed: 15508168]

Basser PJ, Jones DK. Diffusion-tensor MRI: theory, experimental design and data analysis–a technical review. NMR Biomed. 2002; 15:456–467. [PubMed: 12489095]

Basser PJ, Mattiello J, LeBihan D. Estimation of the effective self-diffusion tensor from the NMR spin echo. J Magn Reson Ser B. 1994a; 103:247–254. [PubMed: 8019776]

Basser PJ, Mattiello J, LeBihan D. MR diffusion tensor spectroscopy and imaging. Biophys J. 1994b; 66:259–267. [PubMed: 8130344]

Beaulieu C. The basis of anisotropic water diffusion in the nervous system–a technical review. NMR Biomed. 2002; 15:435–455.10.1002/nbm.782 [PubMed: 12489094]

Beaulieu CF, Zhou X, Cofer GP, Johnson GA. Diffusion-weighted MR microscopy with fast spin-echo. Magn Reson Med. 1993; 30:201–206. [PubMed: 8366801]

Benitez A, Fieremans E, Jensen JH, Falangola MF, Tabesh A, Ferris SH, Helpern JA. White matter tract integrity metrics reflect the vulnerability of late-myelinating tracts in Alzheimer's disease. Neuro Image: Clinical. 2014; 4:64–71.10.1016/j.nicl.2013.11.001

Blockx I, De Groof G, Verhoye M, Van Audekerke J, Raber K, Poot D, Sijbers J, Osmand AP, Von Hörsten S, Van der Linden A. Microstructural changes observed with DKI in a transgenic Huntington rat model: evidence for abnormal neurodevelopment. Neuro Image. 2012; 59:957–967. [PubMed: 21906685]

Carson RP, Fu C, Winzenburger P, Ess KC. Deletion of Rictor in neural progenitor cells reveals contributions of mTORC2 signaling to tuberous sclerosis complex. Hum Mol Genet. 2013; 22:140–152.10.1093/hmg/dds414 [PubMed: 23049074]

Carson RP, Van Nielen DL, Winzenburger PA, Ess KC. Neuronal and glia abnormalities in Tsc1-deficient forebrain and partial rescue by rapamycin. Neurobiol Dis. 2012; 45:369–380.10.1016/j.nbd.2011.08.024 [PubMed: 21907282]

Cheung MM, Hui ES, Chan KC, Helpern JA, Qi L, Wu EX. Does diffusion kurtosis imaging lead to better neural tissue characterization? A rodent brain maturation study. Neuro Image. 2009; 45:386–392.10.1016/j.neuroimage.2008.12.018 [PubMed: 19150655]

Davis KL, Stewart DG, Friedman JI, Buchsbaum M, Harvey PD, Hof PR, Buxbaum J, Haroutunian V. White matter changes in schizophrenia: evidence for myelin-related dysfunction. Arch Gen Psychiat. 2003; 60:443–456.10.1001/archpsyc.60.5.443 [PubMed: 12742865]

Dortch RD, Apker GA, Valentine WM, Lai B, Does MD. Compartment-specific enhancement of white matter and nerve ex vivo using chromium. Magn Reson Med. 2010; 64:688–697.10.1002/mrm.22460 [PubMed: 20806376]

Falangola MF, Guilfoyle DN, Tabesh A, Hui ES, Nie X, Jensen JH, Gerum SV, Hu C, LaFrancois J, Collins HR, Helpern JA. Histological correlation of diffusional kurtosis and white matter modeling metrics in cuprizone-induced corpus callosum demyelination. NMR Biomed. 2014; 27:948–957.10.1002/nbm.3140 [PubMed: 24890981]

Fieremans E, Benitez A, Jensen JH, Falangola MF, Tabesh A, Deardorff RL, Spampinato MVS, Babb JS, Novikov DS, Ferris SH, Helpern JA. Novel white matter tract integrity metrics sensitive to Alzheimer disease progression. Am J Neuroradiol. 2013; 34:2105–2112.10.3174/ajnr.A3553 [PubMed: 23764722]

Fieremans, E.; Jensen, JH.; Helpern, JA.; Kim, S.; Grossman, R.; Inglese, M. Diffusion distinguishes between axonal loss and demyelination in brain white matter. 20th Annual Meeting of the International Society for Magnetic Resonance in Medicine; Melbourne, Australia. 2012a. p. 465

Fieremans, E.; Jensen, JH.; Hui, ES.; Novikov, DS.; Tabesh, A.; Bonilha, L. Direct evidence for decreased intra-axonal diffusivity in ischemic human stroke. 20th Annual Meeting of the International Society for Magnetic Resonance in Medicine; Melbourne, Australia. 2012b. p. 3600

Fieremans E, Jensen JH, Helpern JA. White matter characterization with diffusional kurtosis imaging. Neuro Image. 2011; 58:177–188.10.1016/j.neuroimage.2011.06.006 [PubMed: 21699989]

Fox CH, Johnson FB, Whiting J, Roller PP. Formaldehyde fixation. J Histochem Cytochem. 1985; 33:845–853. [PubMed: 3894502]

Gochberg DF, Gore JC. Quantitative magnetization transfer imaging via selective inversion recovery with short repetition times. Magn Reson Med. 2007; 57:437–441. [PubMed: 17260381]

Helpern JA, Adisetiyo V, Falangola MF, Hu C, Di Martino A, Williams K, Castellanos FX, Jensen JH. Preliminary evidence of altered gray and white matter microstructural development in the frontal lobe of adolescents with attention-deficit hyperactivity disorder: A diffusional kurtosis imaging study. J Magn Reson Imaging. 2011; 33:17–23.10.1002/jmri.22397 [PubMed: 21182116]

Hennig J. Multiecho imaging sequences with low refocusing flip angles. J Magn Reson. 1988; 78:397–407.

Hui ES, Fieremans E, Jensen JH, Tabesh A, Feng W, Bonilha L, Spampinato MV, Adams R, Helpern JA. Stroke assessment with diffusional kurtosis imaging. Stroke. 2012; 43:2968–2973.10.1161/STROKEAHA.112.657742 [PubMed: 22933581]

Hui ES, Cheung MM, Qi L, Wu EX. Towards better MR characterization of neural tissues using directional diffusion kurtosis analysis. Neuro Image. 2008; 42:122–134. [PubMed: 18524628]

Jensen JH, Helpern JA. MRI quantification of non-Gaussian water diffusion by kurtosis analysis. NMR Biomed. 2010; 23:698–710.10.1002/nbm.1518 [PubMed: 20632416]

Jensen JH, Helpern JA, Ramani A, Lu H, Kaczynski K. Diffusional kurtosis imaging: The quantification of non-gaussian water diffusion by means of magnetic resonance imaging. Magn Reson Med. 2005; 53:1432–1440.10.1002/mrm.20508 [PubMed: 15906300]

Johnson GA, Cofer GP, Gewalt SL, Hedlund LW. Morphologic phenotyping with MR microscopy: the visible mouse. Radiology. 2002; 222:789–793.10.1148/radiol.2223010531 [PubMed: 11867802]

Jones DK, Horsfield MA, Simmons A. Optimal strategies for measuring diffusion in anisotropic systems by magnetic resonance imaging. Magn Reson Med. 1999; 42:515–525. [PubMed: 10467296]

Karnovsky MJ. A formaldehyde-glutaraldehyde fixative of high osmolality for use in electron microscopy. J Cell Biol. 1965; 27:137A–138A.

Koenig SH, Brown RD, Spiller M, Lundbom N. Relaxometry of brain: why white matter appears bright in MRI. Magn Reson Med. 1990; 14:482–495. [PubMed: 2355830]

Kucharczyk W, Macdonald PM, Stanisz GJ, Henkelman RM. Relaxivity and magnetization transfer of white matter lipids at MR imaging: importance of cerebrosides and pH. Radiology. 1994; 192:521–529. [PubMed: 8029426]

Landman BA, Farrell JA, Jones CK, Smith SA, Prince JL, Mori S. Effects of diffusion weighting schemes on the reproducibility of DTI-derived fractional anisotropy, mean diffusivity, and principal eigenvector measurements at 1.5 T. Neuro Image. 2007; 36:1123–1138. [PubMed: 17532649]

Lawson, CL.; Hanson, RJ. Solving least squares problems. Prentice-Hall; Englewood Cliffs, NJ: 1974.

Le Bihan D, Mangin JF, Poupon C, Clark CA, Pappata S, Molko N, Chabriat H. Diffusion tensor imaging: concepts and applications. J Magn Reson Imaging. 2001; 13:534–546. [PubMed: 11276097]

Lee CY, Tabesh A, Benitez A, Helpern JA, Jensen JH, Bonilha L. Microstructural integrity of early- versus late-myelinating white matter tracts in medial temporal lobe epilepsy. Epilepsia. 2013; 54:1801–1809. [PubMed: 24032670]

Lu H, Jensen JH, Ramani A, Helpern JA. Three-dimensional characterization of non-gaussian water diffusion in humans using diffusion kurtosis imaging. NMR Biomed. 2006; 19:236–247.10.1002/nbm.1020 [PubMed: 16521095]

MacKay A, Whittall K, Adler J, Li D, Paty D, Graeb D. In vivo visualization of myelin water in brain by magnetic resonance. Magn Reson Med. 1994; 31:673–677. [PubMed: 8057820]

Mädler B, Drabycz SA, Kolind SH, Whittall KP, MacKay AL. Is diffusion anisotropy an accurate monitor of myelination?: Correlation of multicomponent T2 relaxation and diffusion tensor anisotropy in human brain. Magn Reson Imaging. 2008; 26:874–888. [PubMed: 18524521]

Mason JL, Langaman C, Morell P, Suzuki K, Matsushima GK. Episodic demyelination and subsequent remyelination within the murine central nervous system: changes in axonal calibre. Neuropath Appl Neuro. 2001; 27:50–58.

Menon RS, Rusinko MS, Allen PS. Proton relaxation studies of water compartmentalization in a model neurological system. Magn Reson Med. 1992; 28:264–274. [PubMed: 1281258]

Neeman M, Freyer JP, Sillerud LO. A simple method for obtaining cross-term-free images for diffusion anisotropy studies in NMR microimaging. Magn Reson Med. 1991; 21:138–143. [PubMed: 1943671]

Paxinos, G.; Franklin, KB. The mouse brain in stereotaxic coordinates. Gulf Professional Publishing; 2004.

Prasloski T, Mädler B, Xiang QS, MacKay A, Jones C. Applications of stimulated echo correction to multicomponent T2 analysis. Magn Reson Med. 2012; 67:1803–1814.10.1002/mrm.23157 [PubMed: 22012743]

Purea A, Webb AG. Reversible and irreversible effects of chemical fixation on the NMR properties of single cells. Magn Reson Med. 2006; 56:927–931.10.1002/mrm.21018 [PubMed: 16941621]

Ramani, A.; Jensen, JH.; Szulc, KU.; Ali, O.; Hu, C.; Lu, H.; Brodle, JD.; Helpern, JA. Assessment of abormalities in the cerebral microstructure of schizophrenia patients: a diffusional kurtosis imaging study. 15th Annual Meeting of the International Society for Magnetic Resonance in Medicine; Berlin, Germany. 2007. p. 648

Shepherd TM, Thelwall PE, Stanisz GJ, Blackband SJ. Aldehyde fixative solutions alter the water relaxation and diffusion properties of nervous tissue. Magn Reson Med. 2009; 62:26–34.10.1002/mrm.21977 [PubMed: 19353660]

Sled JG, Pike GB. Quantitative interpretation of magnetization transfer in spoiled gradient echo MRI sequences. J Magn Reson. 2000; 145:24–36.10.1006/jmre.2000.2059 [PubMed: 10873494]

Song SK, Sun SW, Ramsbottom MJ, Chang C, Russell J, Cross AH. Dysmyelination revealed through MRI as increased radial (but unchanged axial) diffusion of water. Neuro Image. 2002; 17:1429–1436.10.1006/nimg.2002.1267 [PubMed: 12414282]

Song SK, Yoshino J, Le TQ, Lin SJ, Sun SW, Cross AH, Armstrong RC. Demyelination increases radial diffusivity in corpus callosum of mouse brain. Neuro Image. 2005; 26:132–140.10.1016/j.neuroimage.2005.01.028 [PubMed: 15862213]

Stikov N, Perry LM, Mezer A, Rykhlevskaia E, Wandell BA, Pauly JM, Dougherty RF. Bound pool fractions complement diffusion measures to describe white matter micro and macrostructure. NeuroImage. 2011; 54:1112–1121. [PubMed: 20828622]

Sun SW, Neil JJ, Song SK. Relative indices of water diffusion anisotropy are equivalent in live and formalin-fixed mouse brains. Magn Reson Med. 2003; 50:743–748. [PubMed: 14523960]

Sun SW, Liang HF, Trinkaus K, Cross AH, Armstrong RC, Song SK. Noninvasive detection of cuprizone induced axonal damage and demyelination in the mouse corpus callosum. Magn Reson Med. 2006; 55:302–308. [PubMed: 16408263]

Tabesh A, Jensen JH, Ardekani BA, Helpern JA. Estimation of tensors and tensor-derived measures in diffusional kurtosis imaging. Magn Reson Med. 2011; 65:823–836.10.1002/mrm.22655 [PubMed: 21337412]

Thiessen JD, Zhang Y, Zhang H, Wang L, Buist R, Del Bigio MR, Kong J, Li XM, Martin M. Quantitative MRI and ultrastructural examination of the cuprizone mouse model of demyelination. NMR Biomed. 2013; 26:1562–1581.10.1002/nbm.2992 [PubMed: 23943390]

Thirion JP. Image matching as a diffusion process: an analogy with Maxwell's demons. Med Image Anal. 1998; 2:243–260. [PubMed: 9873902]

Whittall KP, MacKay AL. Quantitative interpretation of NMR relaxation data. J Magn Reson. 1989; 84:134–152.

Wu EX, Cheung MM. MR diffusion kurtosis imaging for neural tissue characterization. NMR Biomed. 2010; 23:836–848.10.1002/nbm.1506 [PubMed: 20623793]

Zhang H, Schneider T, Wheeler-Kingshott CA, Alexander DC. NODDI: practical in vivo neurite orientation dispersion and density imaging of the human brain. NeuroImage. 2012; 61:1000–1016. [PubMed: 22484410]

Zhang J, Jones MV, McMahon MT, Mori S, Calabresi PA. In vivo and ex vivo diffusion tensor imaging of cuprizone-induced demyelination in the mouse corpus callosum. Magn Reson Med. 2012; 67:750–759.10.1002/mrm.23032 [PubMed: 21656567]

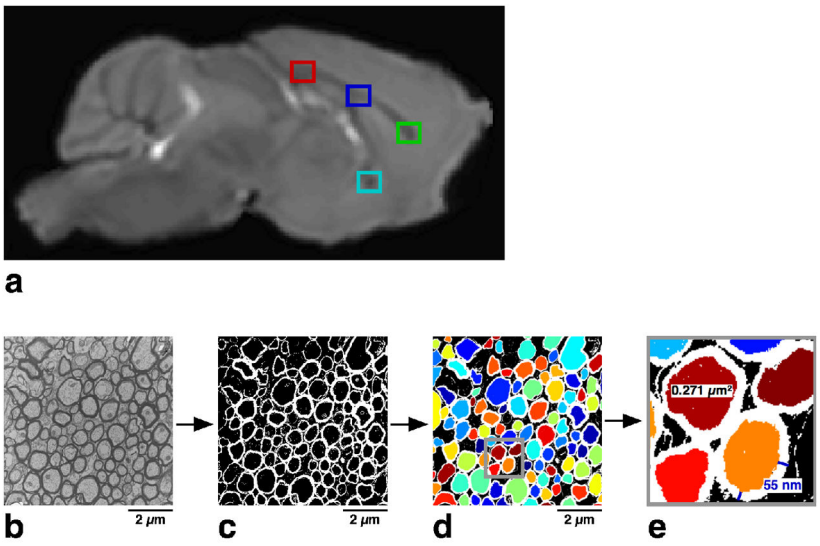

FIG. 1.

Quantitative histology metrics derived from EM. (a) T_2-weighted sagittal cross-section showing locations of white matter histology sections. (b) Typical 15000x EM image of the splenium. (c) EM image after segmentation with myelin pixels shown in white. (d) EM image showing axons after region growing segmentation is performed to derive axon area and diameter. (e) Typical axon area and z_m measurements.

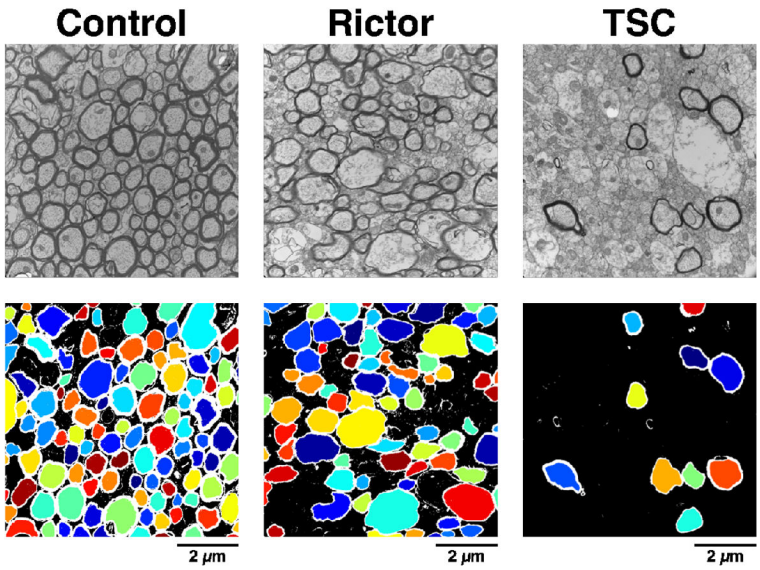

FIG. 2.

Representative EM images of white matter. (Top row) EM images of the splenium from control, Rictor and TSC mouse brains. (Bottom row) Processed and segmented EM images corresponding to the images shown on the top row. Compared to the control brain, Rictor brain WM shows a slight decrease in myelin thickness and myelinated axon density. TSC brain WM shows a significant decrease in myelinated axon density.

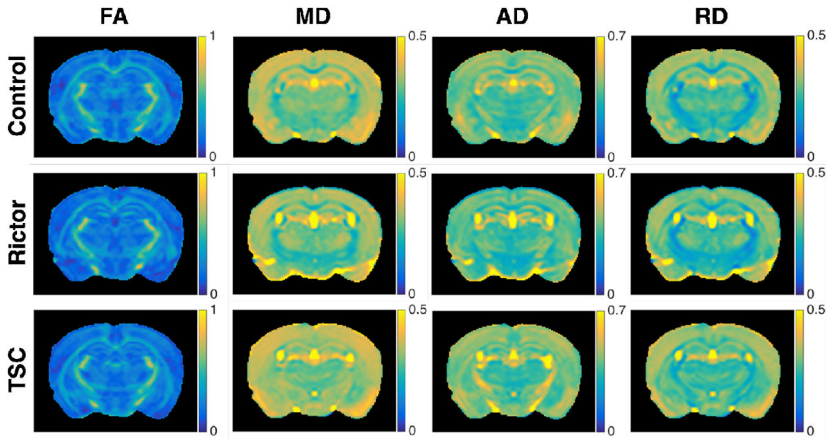

FIG. 3.

Representative coronal DTI parameter maps. The rows represent the three groups: control (top), Rictor (middle), and TSC (bottom). The columns represent the DTI parameters FA, MD, AD, and RD. FA is unitless and diffusivities are in units of $\mu m^2/ms$.

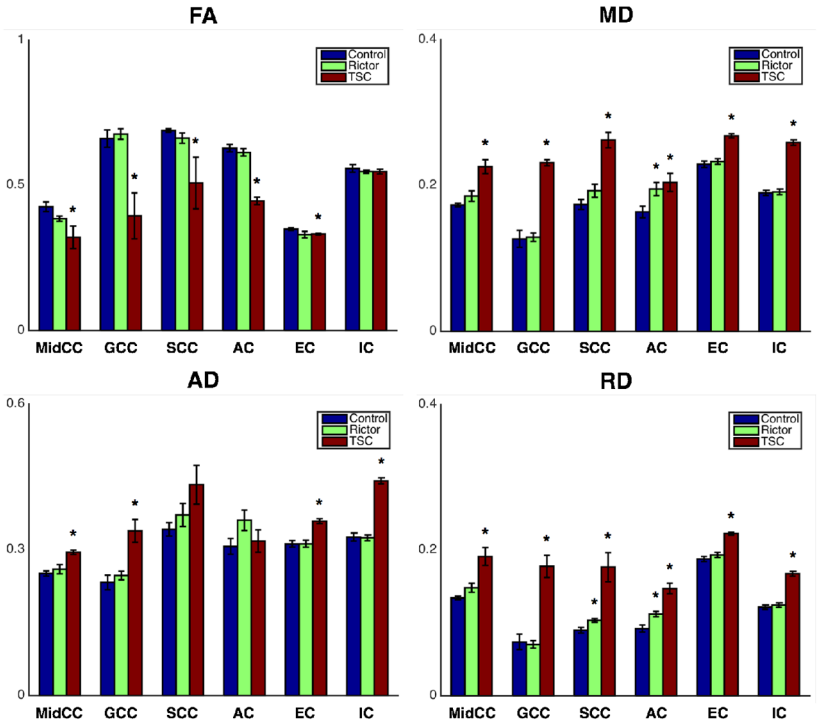

FIG. 4.

ROI group comparison of DTI parameters FA, MD, AD, and RD. Bar heights represent the ROI parameter means across each group, with error bars spanning the mean ± SEM. The three groups are represented with different colors: control = blue, Rictor = green, and TSC = red. 6 WM ROIs are indicated on the x-axis: MidCC = midbody of the corpus callosum, GCC = genu, SCC = splenium, AC = anterior commissure, EC = external capsule, and IC = internal capsule. FA is unitless and diffusivities are in units of $\mu m^2/ms$. * denotes $p < 0.05$ for comparison between the control group and each CKO group.

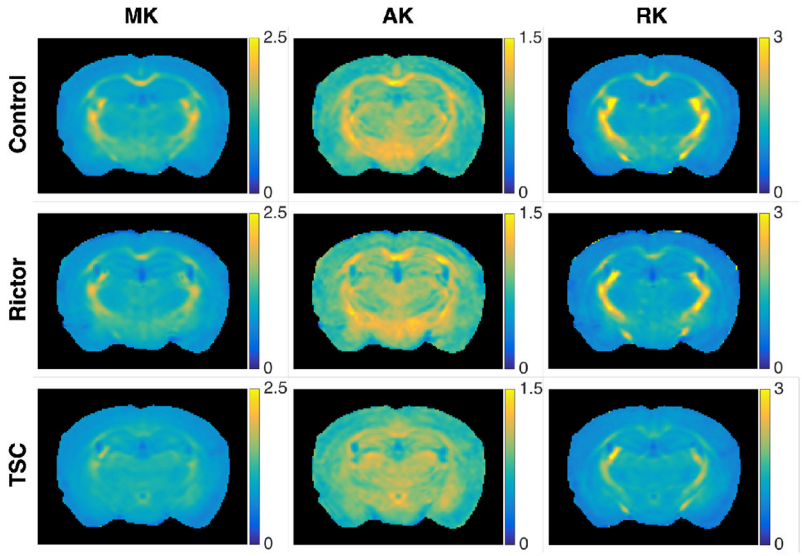

FIG. 5.

Representative coronal DKI parameter maps. The rows represent the three groups: control (top), Rictor (middle), and TSC (bottom). The columns represent the DKI parameters MK, AK, and RK. Kurtosis is unitless.

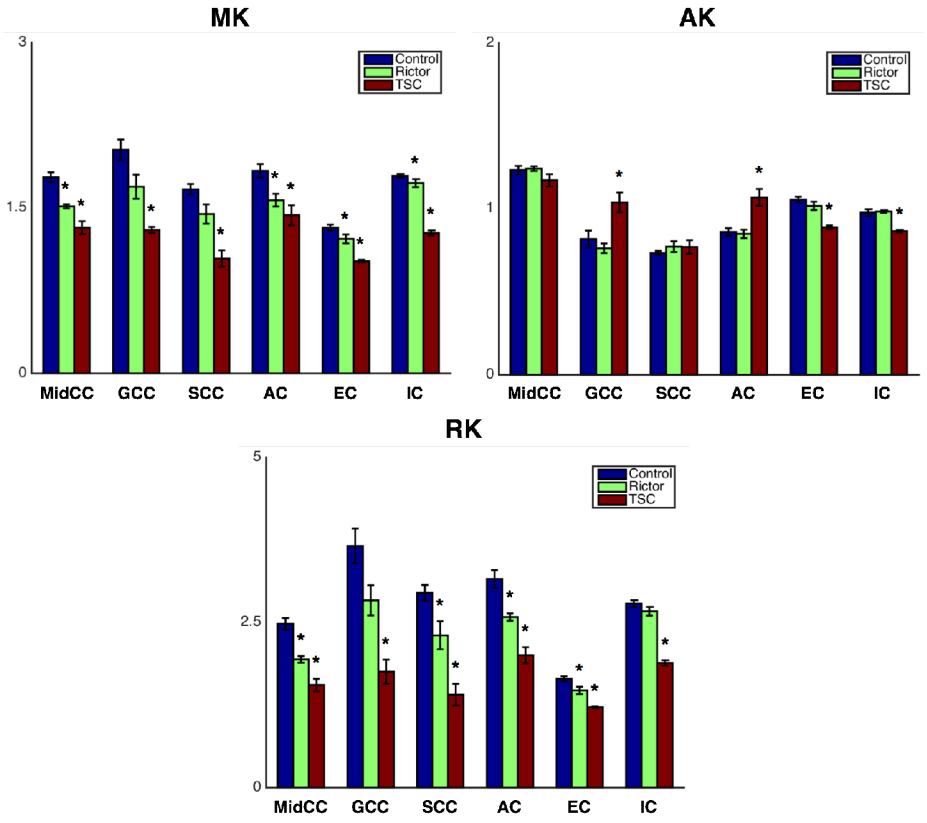

FIG. 6.

ROI group comparison of DKI parameters MK, AK, and RK. Bar heights represent the ROI parameter means across each group, with error bars spanning the mean ± SEM. The three groups are represented with different colors: control = blue, Rictor = green, and TSC = red. 6 WM ROIs are indicated on the x-axis: MidCC = midbody of the corpus callosum, GCC = genu, SCC = splenium, AC = anterior commissure, EC = external capsule, and IC = internal capsule. Kurtosis is unitless. * denotes $p < 0.05$ for comparison between the control group and each CKO group.

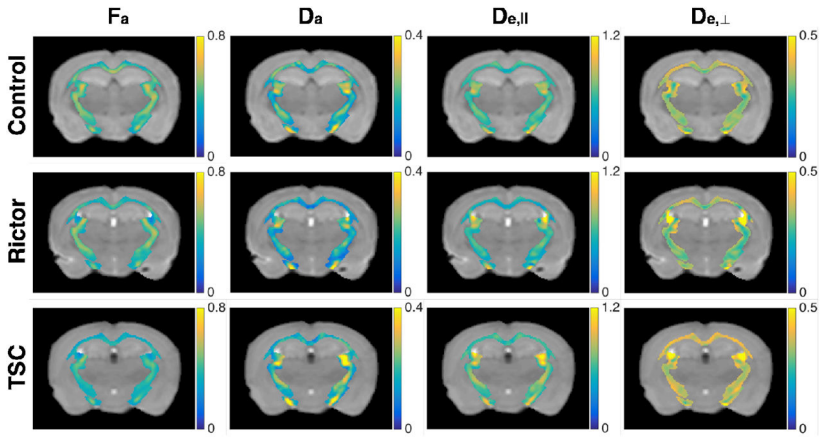

FIG. 7.

Representative coronal WMTI parameter maps. WMTI parameter values for white matter voxels are overlaid on the b=0 image. The rows represent the three groups: control (top), Rictor (middle), and TSC (bottom). The columns represent the WMTI parameters F_a, D_a, $D_{e,\parallel}$, and $D_{e,\perp}$. F_a is unitless and diffusivities are in units of $\mu m^2/ms$.

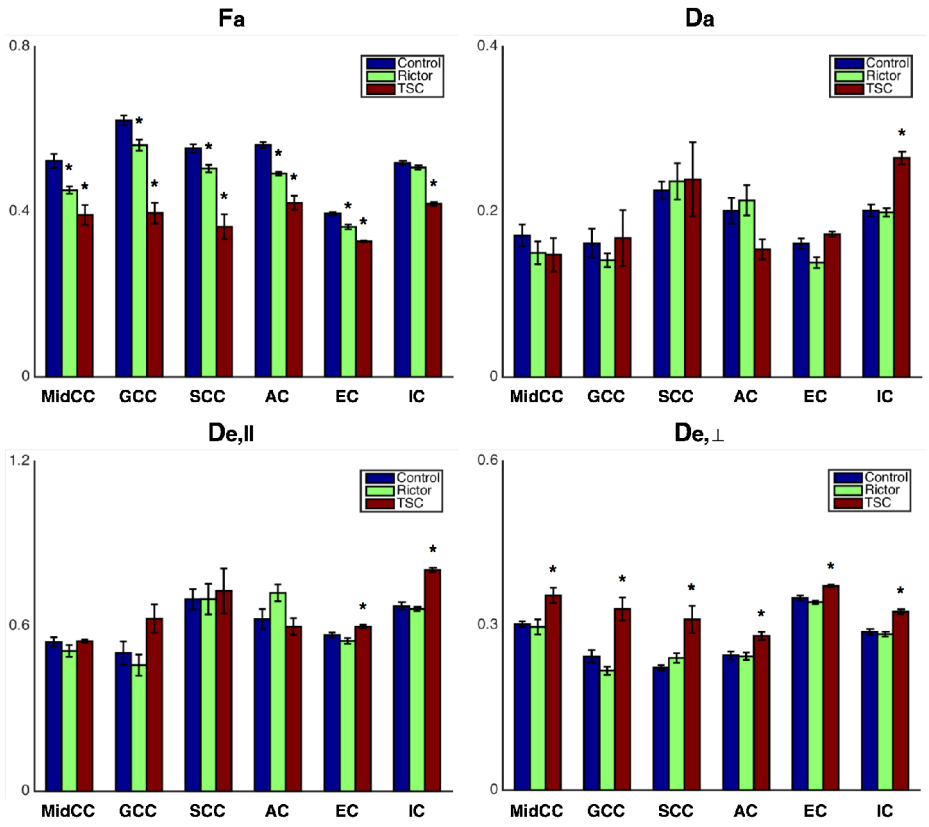

FIG. 8.

ROI group comparison of WMTI parameters F_a, D_a, $D_{e,\parallel}$, and $D_{e,\perp}$. Bar heights represent the ROI parameter means across each group, with error bars spanning the mean ± SEM. The three groups are represented with different colors: control = blue, Rictor = green, and TSC = red. 6 WM ROIs are indicated on the x-axis: MidCC = midbody of the corpus callosum, GCC = genu, SCC = splenium, AC = anterior commissure, EC = external capsule, and IC = internal capsule. F_a is unitless and diffusivities are in units of $\mu m^2/ms$. * denotes $p < 0.05$ for comparison between the control group and each CKO group.

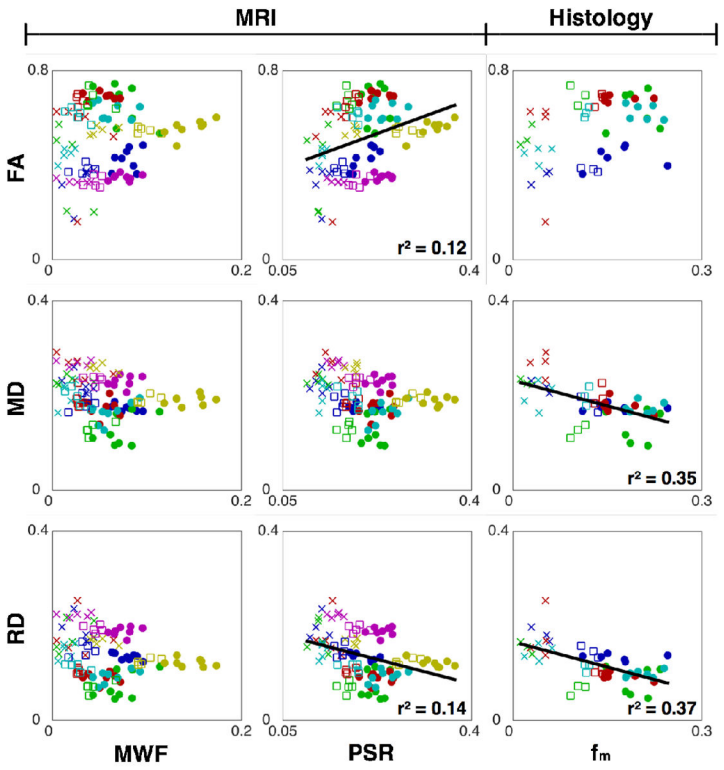

FIG. 9.

Linear correlation plots between DTI metrics FA, MD, and RD (y-axis) and myelin measures MWF, PSR, and f_m (x-axis). Each point is an ROI mean from an individual mouse brain. The shape represents the group: control = circle, Rictor = square, and TSC = x and the color represents the WM region: MidCC = blue, GCC = green, SCC = red, AC = cyan, EC = magenta, IC = yellow. For significant correlations, r^2 is shown in the lower right-hand corner of each plot. FA, MWF, PSR, and f_m are unitless, MD and RD are in units of $\mu m^2/ms$.

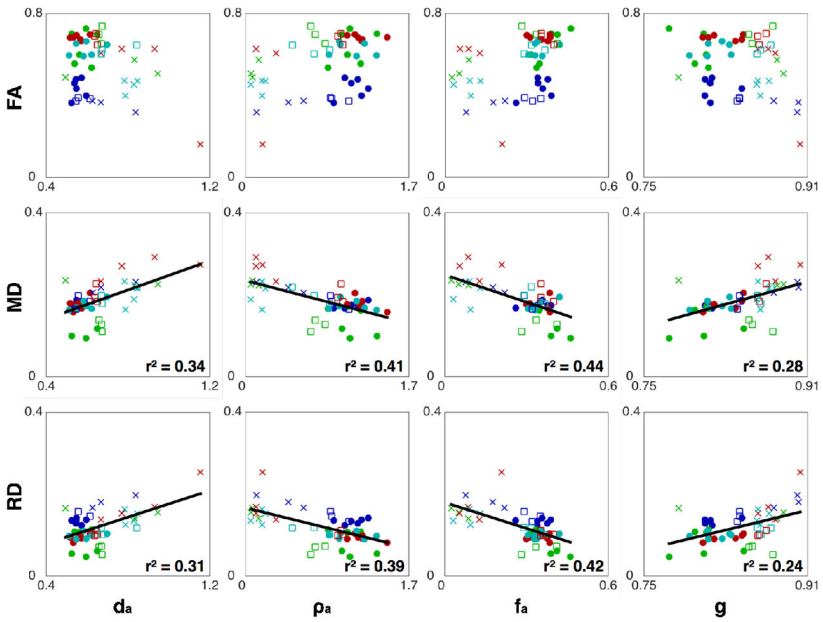

FIG. 10.

Linear correlation plots between DTI metrics FA, MD, and RD (y-axis) and the histologic measures d_a, ρ_a, f_a, and g (x-axis). Each point is an ROI mean from an individual mouse brain. The shape represents the group: control = circle, Rictor = square, and TSC = x and the color represents the WM region: MidCC = blue, GCC = green, SCC = red, AC = cyan. For significant correlations, r^2 is shown in the lower right-hand corner of each plot. FA, f_a, and g are unitless, MD and RD are in units of $\mu m^2/ms$, d_a is in units of μm, and ρ_a is in units of axons/μm^2.

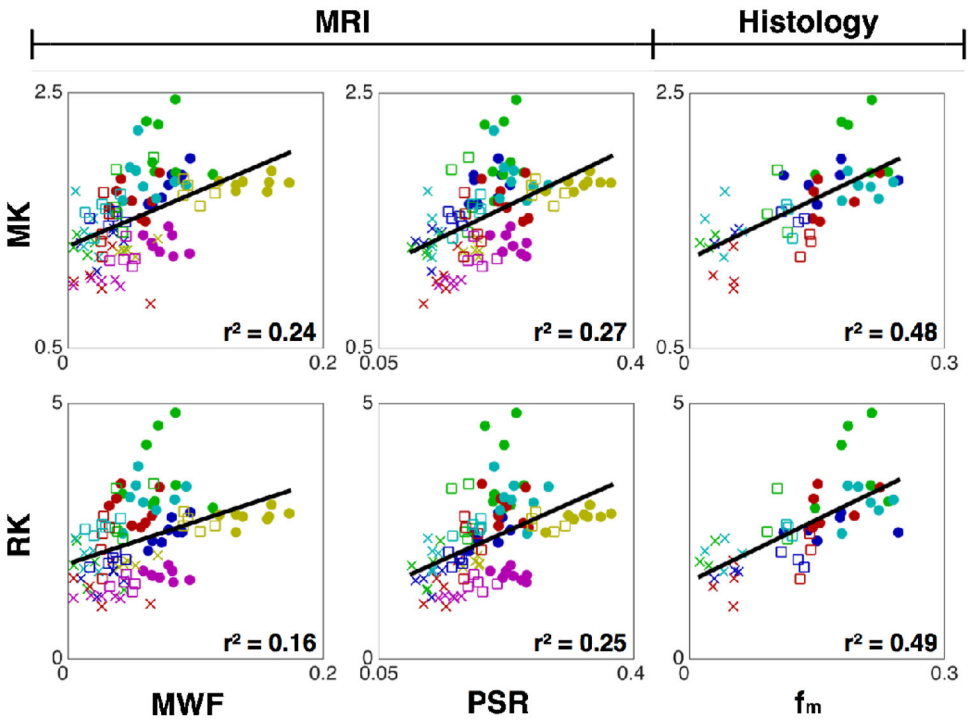

FIG. 11.

Linear correlation plots between DKI metrics MK and RK (y-axis) and myelin measures MWF, PSR, and f_m (x-axis). Each point is an ROI mean from an individual mouse brain. The shape represents the group: control = circle, Rictor = square, and TSC = x and the color represents the WM region: MidCC = blue, GCC = green, SCC = red, AC = cyan, EC = magenta, IC = yellow. For significant correlations, r^2 is shown in the lower right-hand corner of each plot. MK, RK, MWF, PSR, and f_m are unitless.

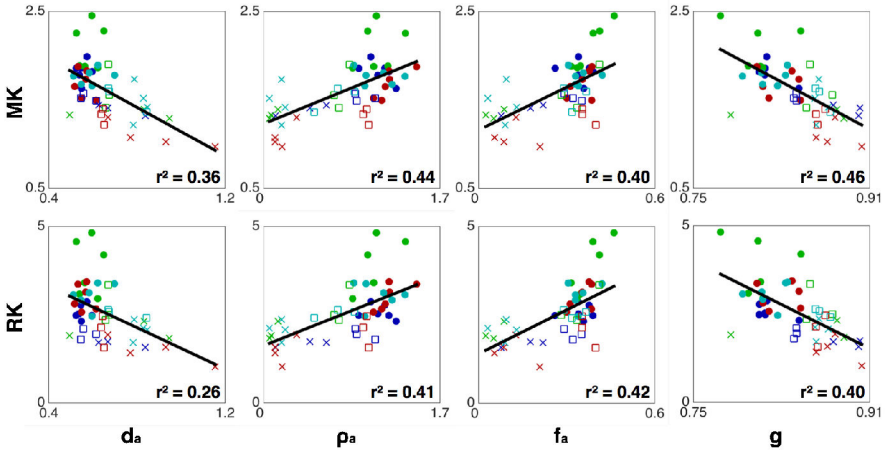

FIG. 12.

Linear correlation plots between DKI metrics MK and RK (y-axis) and the histologic measures d_a, ρ_a, f_a, and g (x-axis). Each point is an ROI mean from an individual mouse brain. The shape represents the group: control = circle, Rictor = square, and TSC = x and the color represents the WM region: MidCC = blue, GCC = green, SCC = red, AC = cyan. For significant correlations, r^2 is shown in the lower right-hand corner of each plot. MK, RK, f_a, and g are unitless, d_a is in units of μm, and ρ_a is in units of axons/μm^2.

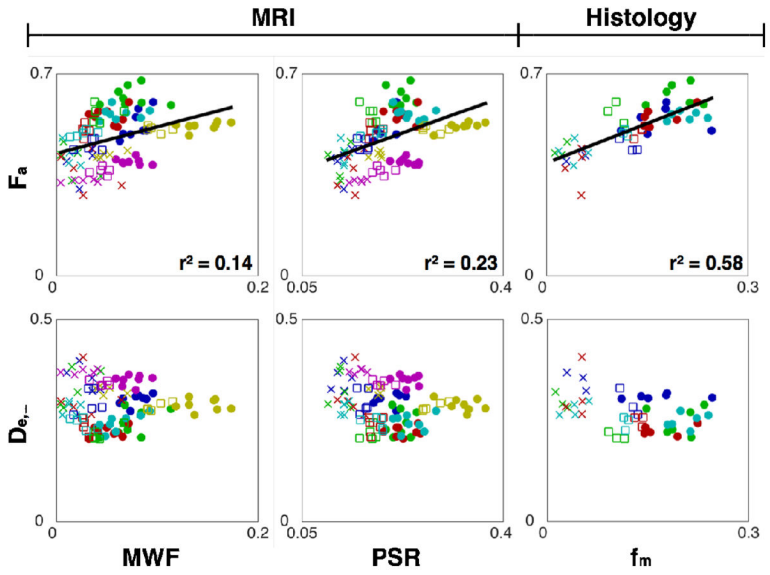

FIG. 13.

Linear correlation plots between WMTI metrics F_a and $D_{e,\perp}$ (y-axis) and myelin measures MWF, PSR, and f_m (x-axis). Each point is an ROI mean from an individual mouse brain. The shape represents the group: control = circle, Rictor = square, and TSC = x and the color represents the WM region: MidCC = blue, GCC = green, SCC = red, AC = cyan, EC = magenta, IC = yellow. For significant correlations, r^2 is shown in the lower right-hand corner of each plot. F_a, MWF, PSR, and f_m are unitless, $D_{e,\perp}$ is in units of $\mu m^2/ms$.

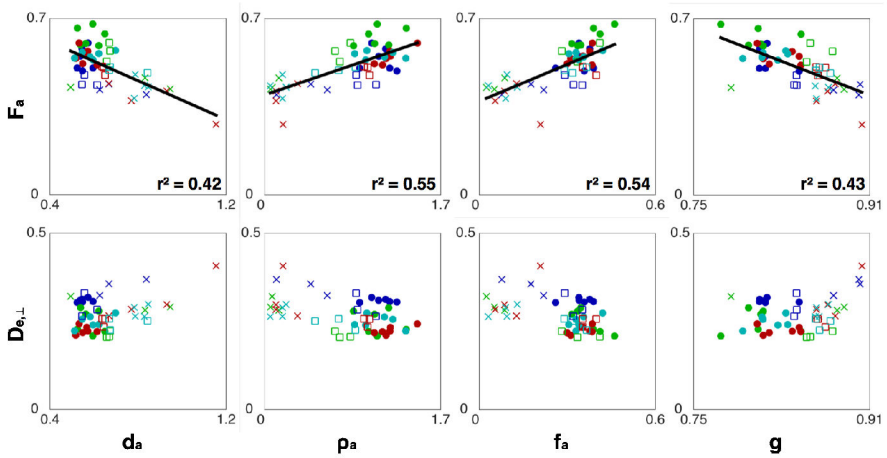

FIG. 14.

Linear correlation plots between WMTI metrics F_a and $D_{e,\perp}$ (y-axis) and the histologic measures d_a, ρ_a, f_a, and g (x-axis). Each point is an ROI mean from an individual mouse brain. The shape represents the group: control = circle, Rictor = square, and TSC = x and the color represents the WM region: MidCC = blue, GCC = green, SCC = red, AC = cyan. For significant correlations, r^2 is shown in the lower right-hand corner of each plot. F_a, f_a, and g are unitless, $D_{e,\perp}$ is in units of $\mu m^2/ms$, d_a is in units of μm, and ρ_a is in units of axons/μm^2.

Table 1

Group mean ± SEM of quantitative histology measures for control, Rictor, and TSC groups.

		f_m	f_a	d_a (μm)	z_m (nm)	g	ρ_a (axons/μm^2)
	Control	0.167 ± 0.022	0.394 ± 0.029	0.558 ± 0.026	55.0 ± 3.1	0.815 ± 0.007	1.124 ± 0.079
MidCC	**Rictor**	0.124 ± 0.025***	0.374 ± 0.047	0.578 ± 0.033	45.2 ± 3.5***	0.844 ± 0.011***	0.945 ± 0.084*
	TSC	0.046 ± 0.011***	0.183 ± 0.049***	0.712 ± 0.134***	36.5 ± 5.1***	0.894 ± 0.014***	0.310 ± 0.113***
	Control	0.196 ± 0.018	0.439 ± 0.023	0.588 ± 0.024	58.7 ± 2.7	0.811 ± 0.010	1.097 ± 0.076
GCC	**Rictor**	0.103 ± 0.019***	0.380 ± 0.050**	0.671 ± 0.033***	44.5 ± 3.2***	0.863 ± 0.012***	0.738 ± 0.084***
	TSC	0.023 ± 0.007***	0.071 ± 0.029***	0.714 ± 0.160**	46.8 ± 5.8***	0.850 ± 0.039***	0.100 ± 0.027***
	Control	0.187 ± 0.019	0.416 ± 0.025	0.560 ± 0.020	51.1 ± 2.4	0.830 ± 0.009	1.205 ± 0.074
SCC	**Rictor**	0.138 ± 0.026**	0.398 ± 0.045	0.647 ± 0.031***	46.1 ± 3.2***	0.866 ± 0.009***	0.989 ± 0.098**
	TSC	0.049 ± 0.017***	0.145 ± 0.049***	0.894 ± 0.132***	56.9 ± 8.2	0.879 ± 0.012***	0.197 ± 0.054***
	Control	0.206 ± 0.023	0.384 ± 0.024	0.600 ± 0.032	60.0 ± 3.3	0.821 ± 0.011	1.094 ± 0.106
AC	**Rictor**	0.117 ± 0.020***	0.376 ± 0.041	0.748 ± 0.069***	52.2 ± 4.9***	0.868 ± 0.010***	0.695 ± 0.114**
	TSC	0.040 ± 0.013***	0.097 ± 0.033***	0.792 ± 0.044***	61.7 ± 7.9	0.862 ± 0.017***	0.152 ± 0.040***

Significant differences compared with the control group are indicated by * ($p \leq 0.05$), ** ($p \leq 0.01$), and *** ($p \leq 0.001$).

Table 2

r^2 values from linear correlation analysis of DTI, DKI, and WMTI metrics.

		DTI				DKI			WMTI			
		FA	**MD**	**AD**	**RD**	**MK**	**AK**	**RK**	F_a	D_a	$D_{e,\|\|}$	$D_{e,\perp}$
MRI	**MWF**					0.24		0.16	0.14			
	PSR	0.12			0.14	0.27		0.25	0.23			
Histology	f_m		0.35		0.37	0.48		0.49	0.58			
	f_a		0.44		0.42	0.40		0.42	0.54			
	d_a		0.34		0.31	0.36		0.26	0.42			
	z_m											
	ρ_a		0.41		0.39	0.44		0.41	0.55			
	g		0.28		0.24	0.46		0.40	0.43			

Only r^2 values for significant correlations ($p < 0.05$) are shown.